RSC Advances

ROYAL SOCIETY OF CHEMISTRY

www.rsc.org/advances

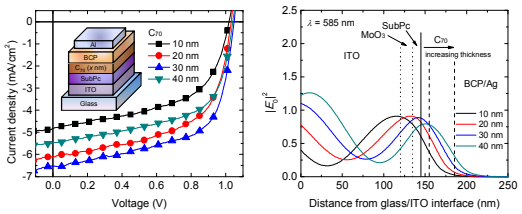

Optimizing performance of fullerene-based small-molecule organic photovoltaic devices by simply changing the fullerene thickness with high V_{OC}, J_{SC}, and FF.

RSC Advances

RSCPublishing

ARTICLE

Decoupling the optical and electrical properties of subphthalocyanine/C_{70} bi-layer organic photovoltaic devices: improved photocurrent while maintaining a high open-circuit voltage and fill factor

Cite this: DOI: 10.1039/x0xx00000x

Received ooth January 2012,
Accepted ooth January 2012

DOI: 10.1039/x0xx00000x

www.rsc.org/

Chih-Chien Lee,[a]*† Wei-Cheng Su,[a] Yi-Sheng Shu,[b] Wen-Chang Chang,[a] Bo-Yao Huang,[a] Ya-Ze Lee,[b] Tsung-Hao Su,[b] Kuan-Ting Chen[a] and Shun-Wei Liu[b]*†

We demonstrate a simple method for achieving high-performance subphthalocyanine (SubPc)/C_{70} bi-layer organic photovoltaic (OPV) devices through the changing of the C_{70} thickness. The optical and electrical properties of the OPV devices were decoupled and could be individually manipulated to obtain a significantly increased short-circuit current density (J_{SC}) without reducing the open-circuit voltage and the fill factor. The thickness-independent electrical property of the C_{70} layer was systematically studied in terms of the dark currents of the OPV devices and the carrier mobilities of the organic layers; the results indicate that the considerable difference in mobility between SubPc and C_{70} is not detrimental, while the optical-field distribution can be optimized by tuning the C_{70} thickness. The power conversion efficiency was improved from 2.7 to 4.2% by optimizing the C_{70} thickness. The optical effect upon the change in the C_{70} thickness was thoroughly investigated by calculating the optical-field profile and the power dissipation inside the OPV devices on the basis of the transfer matrix method. The calculated results suggest that the optical-field intensity is insufficient in predicting the trend in J_{SC}. Instead, the power dissipation involving the absorption properties of materials and the optical-field distribution of OPV devices can provide deeper insight into the optical condition and indicates the importance of optimizing the film thickness in bi-layer OPV devices.

Introduction

Organic photovoltaic (OPV) devices have exhibited potential for commercialization as the device efficiency significantly improves and the compatibility of flexible, large-area substrates by a low-cost and high-volume processing develops.[1-4] In the state of the art, several groups have reported a power conversion efficiency (PCE) exceeding 7% for polymer solar cells (PSCs) with the use of structural design and/or novel materials,[5-7] permitting the achievement of the theoretical maximum of over 10%.[8, 9] Fabrication processes scaling up from single tandem cells to modules of fully roll-to-roll printing indium-free flexible devices and the enhancement via encapsulation of the operating lifetime under worldwide outdoor testing indicate that the PSCs can now be used in realistic applications.[10-13]

By contrast, the PCE of small-molecule OPV devices is lagging behind the PCE of the PSCs due to the inferior carrier transport (which depends on the molecular packing) and the limited absorption band over the spectral coverage, as reflected by a relatively low short-circuit current density (J_{SC}) and fill factor (FF).[14, 15] Since the first efficient OPV device was proposed,[16] many efforts have been devoted to improve the device performance.[17-19] A huge progress was made in recent years. Several groups have demonstrated the small-molecule OPV devices with PCE of over 7% and even 10%,[20-26] thus indicating the potential use in solar harvesting. In addition, the nature of the large energy gap in small molecules can increase the open-circuit voltage (V_{OC}) because it is mainly determined by the energetic difference between the highest occupied molecular orbital (HOMO) of the donor and the lowest unoccupied molecular orbital (LUMO) of the acceptor.[27] To maintain V_{OC} while enhancing J_{SC} simultaneously, the co-evaporation of donor and acceptor materials forming the so-called bulk heterojunction (BHJ) was demonstrated to significantly increase the interfacial area between donor/acceptor where the exciton dissociation occurs, allowing for the generation of more photo-generated carriers for a higher photocurrent.[28-30] The further improvements of device performance and developments of the device structure design are expected to promote commercialization of small-molecule OPV devices because of the high reproducibility, ease of synthesis and purification, and high compatibility of fabrication process.[31-36]

Although the BHJ can improve the J_{SC} by increasing the dissociation interface as generally demonstrated in PSCs, an

imperfect interpenetrating network between the donor and the acceptor may increase the carrier recombination as a result of the disordered transport path.[37-39] The enhanced carrier recombination often comes at the expense of decreasing FF, which, in addition to V_{OC} and J_{SC}, determines the PCE, especially in the tandem devices in which the FF is commonly close to the value of the limiting cell.[5, 40-42] To overcome this limitation of decreasing FF, the active layer thickness of small-molecule OPV devices is typically less than 60 nm.[25, 26, 43, 44] In such thin films, the optical effects caused by the optical interference become important because it is preferable to place a high amount of absorbed energy into the region having a high possibility of exciton dissociation.[45, 46] Therefore, the thickness optimization should account for both the electrical and optical properties to avoid the trade-off between J_{SC} and FF, thus complicating the device optimization procedure.[18, 47-50]

Alternatively, an optical spacer is a type of material featuring high transparency and conductivity, which can manipulate the optical condition for OPV devices without affecting the electrical properties. Optical spacers, including metal oxides and doped organic layers, are used to enhance light absorption and/or control the absorbing zone of tandem cells.[51-55] However, it is argued that the use of an optical spacer is not required if the active layer thickness of a device is well optimized.[56] Therefore, a deeper understanding and simple analysis of optimizing the active layer thickness is essential before introducing the optical spacer to enhance photocurrent. Here, we demonstrate a simple means to optimize the active layer thickness of a small-molecule bi-layer device by decoupling the optical and electrical properties with the change in the acceptor thickness. Our results indicate that the thickness-independent electrical property of an acceptor with high carrier mobility allows for a significant tuning of optical-field distribution without a reduction in the electrical properties, thereby increasing the J_{SC} while maintaining the high V_{OC} and FF, leading to an increased PCE from 2.7 to 4.2% without additional techniques or structural designs. The calculation of power dissipation at the donor/acceptor interface agrees well with the experimentally observed trend in J_{SC}, demonstrating that the prediction of an optimized active layer thickness is valuable and feasible in bi-layer OPV devices.

Results and discussion

Fig. 1(a) shows the energy level diagram of the OPV devices and the molecular structures of the organic materials. The HOMO and LUMO levels estimated here are in good agreement with the data reported by other groups.[57-62] Because the subphthalocyanine (SubPc) has a relatively low-lying HOMO level, the transition metal oxide MoO_3 is generally used to cover the bare indium-tin-oxide (ITO) thin film for efficient hole extraction without deteriorating the absorption of active layer by virtue of its high transparency.[59, 63] However, extensive studies have demonstrated the potential of high V_{OC} OPV devices by using SubPc as the donor material.[58, 64, 65] The use of C_{70} to be the acceptor material affords the better Fig. of merit than the commonly used C_{60} because C_{70} possesses a higher absorption coefficient and comparable electronic configuration to C_{60}.[28, 60, 66] A thin layer of bathocuproine (BCP) with an appropriate thickness inserted between the acceptor and cathode can reduce the exciton quenching and improve the electron extraction.[67, 68]. Fig. 1(b) shows the optical constants of the organic materials used in this study. As observed in the bottom half of the Fig., the SubPc exhibits two distinct features, with a peak at 585 nm and a shoulder at approximately 535 nm, while C_{70} has a lower but broader absorption in the wavelength range of 400 to 600 nm. The extraordinarily high extinction coefficient of SubPc in combination with the complementary absorption of C_{70} enables a large increase in the photocurrent of OPV devices. However, the nature of the thin film property in OPV devices requires accounting for the optical interference, which can have a significant impact on the photon absorption and hence the J_{SC}.[69, 70] Therefore, deeper insight into the optical manipulation is of great importance to improve the performance of OPV devices.

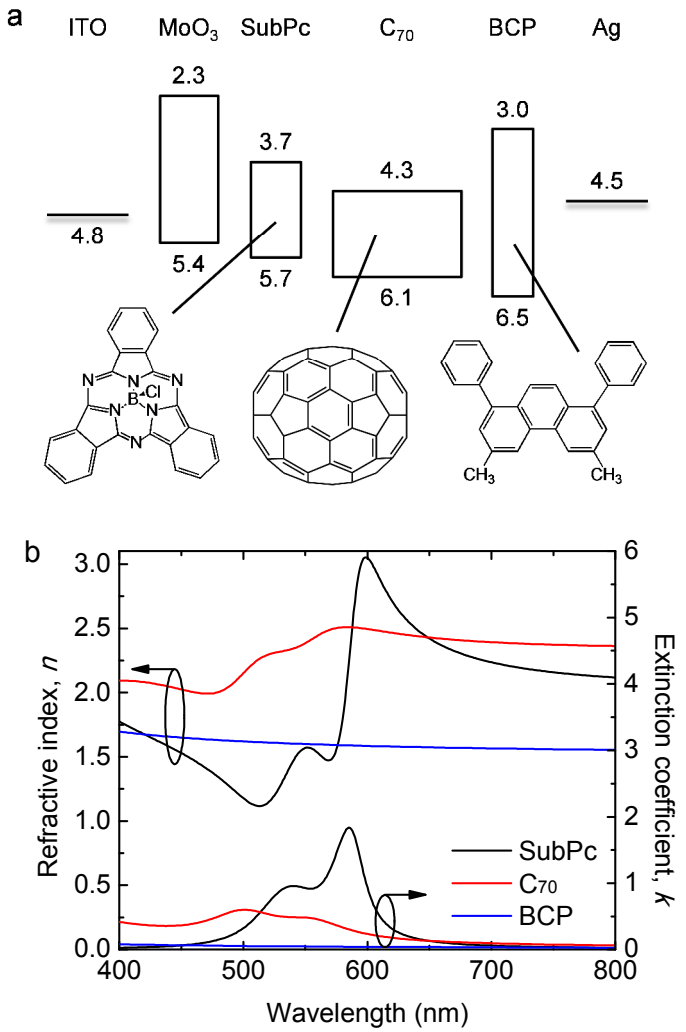

Fig. 1. (a) Energy level diagram of the OPV device in units of eV and the chemical structures of the organic materials. (b) Optical constants of the organic materials.

Optical manipulation is generally controlled by using an optical spacer with high transparency and high electrical conductance.[51, 52, 71, 72] Alternatively, the thickness of the active layer can significantly impact the absorption property in OPV devices. The electrical properties, however, are simultaneously altered by the active layer thickness; hence, the optimization of the performance usually involves a trade-off between J_{SC} and FF.[47, 48, 50] In a bi-layer OPV device with ITO as the anode and a thick metal as the cathode, i.e., the bottom-absorbing configuration, the first optical interference maximum is physically dominated by the reflective metal and peaks at a

position close to the cathode.[73, 74] This characteristic offers the possibility of manipulating the optical-field distribution by changing the thickness of the acceptor with a thickness-independent electrical property.[75] Fig. 2(a) shows the dark current density-voltage (*J-V*) curves of the OPV devices with varied thicknesses of C_{70} in a structure of ITO/MoO_3 (15 nm)/SubPc (10 nm)/C_{70} (*x* nm)/BCP (8 nm)/Ag (100 nm), where *x* is 10, 20, 30, and 40. The changeless forward current is observed, except for the device with the thinnest C_{70}, which may have yet to form a homogeneous film and therefore increases the series resistance as a result of the direct contact of SubPc and BCP. As shown in the inset of Fig. 2(a), the diode behaviors of all devices are almost identical, indicating the possibility to adjust the C_{70} thickness to control the optical-field distribution without affecting the electrical property. Detailed analyses of the diode behaviors are described in the ESI‡ (Section S1). To further investigate the unchanged electrical property, we fabricated hole- and electron-only devices to determine the hole and electron mobilities of SubPc and C_{70}, respectively, based on the space-charge limited current (SCLC), as expressed by[76, 77]

$$J_{SCLC} = \frac{9}{8}\varepsilon\varepsilon_0\mu\frac{E^2}{L}, \qquad (1)$$

where ε and ε_0 are the relative dielectric constant and the permittivity of the free space, respectively, μ is the carrier mobility, and L is the thickness of the organic layer. The structures for hole- and electron-only devices consist of ITO/MoO_3 (15 nm)/SubPc (150 nm)/Au and Al/C_{70} (150 nm)/LiF (1 nm)/Al, respectively. Fig. 2(b) shows the results obtained from SCLCs. The hole and electron mobilities of SubPc and C_{70} are on the order of ~ 10^{-5} cm^2/V-s and ~ 10^{-3} cm^2/V-s, respectively. Note that the hole mobility obtained here is quite different form the result reported by Pandey *et al.*, indicating the value on the order of 10^{-8} cm^2 V^{-1} s^{-1}.[78] This discrepancy is attributed to the differences in the material and sample preparation, such as the purity and/or deposition rate, as observed in the literature.[79-83] The estimated electron mobility of C_{70} here is consistent with the previous reports, revealing an order of magnitude lower than C_{60}.[38, 78, 84] As a result, the device resistance may be mainly dominated by SubPc due to its relatively low carrier mobility, permitting a less significant influence of C_{70} thickness on electrical property.

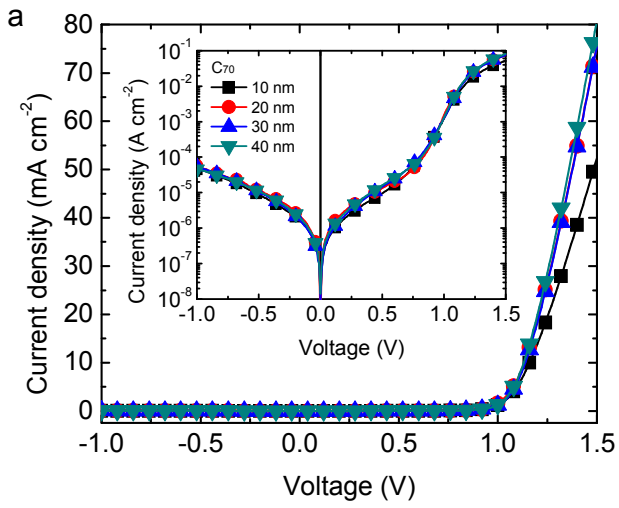

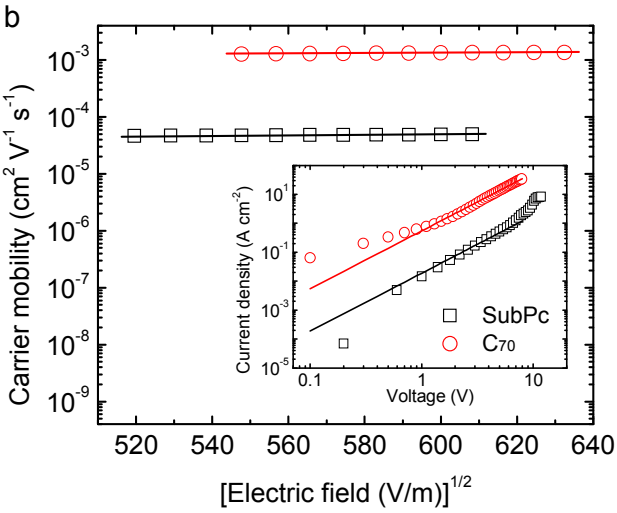

Fig. 2. (a) Dark currents of the OPV devices with varied C_{70} thicknesses in the structure of ITO/MoO_3 (15 nm)/SubPc (10 nm)/C_{70}/BCP (8 nm)/Ag (100 nm). The inset is the semi-log plot. (b) Hole and electron mobilities of SubPc and C_{70}, respectively, as a function of the square root of the electric field. The inset is the SCLCs of the hole- and electron-only devices. Open symbols are the experimental data, and solid lines are the corresponding fits.

The performances under AM 1.5G solar illumination at 100 mW cm^{-2} for the OPV devices with various C_{70} thicknesses are shown in Fig. 3(a). Error bars representing the standard deviation at each data point are also given. Table 1 summarizes the photovoltaic performances on an average of 10 devices for each cell parameter. Because the V_{OC} is mainly determined by the donor/acceptor interface, such as the energy level distribution,[85, 86] bimolecular recombination,[87, 88] and charge transfer dynamics,[89, 90] we obtain similar values for all devices. The J_{SC}, which is of special interest here, exhibits a large difference between these devices: it increases with C_{70} thickness from 10 to 30 nm and then decreases at 40 nm. We ascribe this improvement to the optimum optical-field distribution inside the device when a proper thickness of C_{70} was used. The FF also exhibits a slight dependence on C_{70} thickness and peaks for the 30-nm device. As a result, the overall PCE is improved from 2.7 to 4.2% by the simultaneous enhancement of V_{OC}, J_{SC}, and FF. To better understand the increased J_{SC}, the EQE spectra of the OPV devices were measured, as shown in Fig. 3(b). The extinction coefficients of the active layers were also compared to clarify the contribution to the EQE. Because the J_{SC} is directly correlated with the photoresponse to the solar spectrum, the device with the 30-nm C_{70} has the highest EQE over the entire visible wavelength range. In addition, a considerable change in the spectral shape indicates that in our case, the J_{SC} is mainly determined by the optical-field distribution instead of the charge collection efficiency.[91, 92] These results highlight the dominance of the thickness optimization in a bi-layer OPV device without the use of an additional optical spacer.

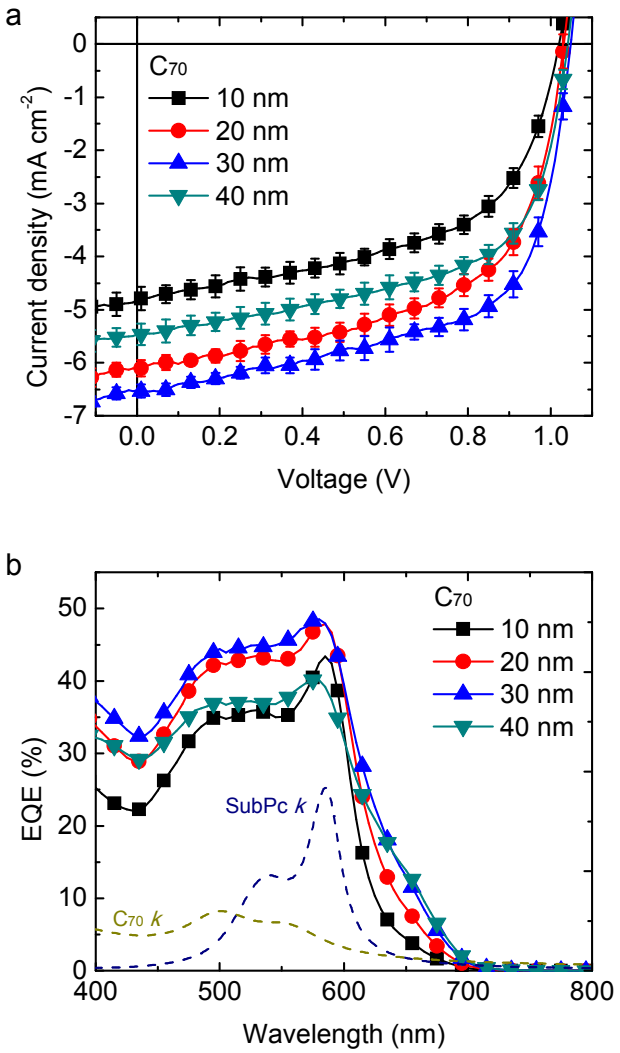

Fig. 3. (a) *J-V* characteristics under AM 1.5G solar illumination at 100 mW cm^{-2} for the OPV devices with different C_{70} thicknesses in the structure of ITO/MoO_3 (15 nm)/SubPc (10 nm)/C_{70}/BCP (8 nm)/Ag (100 nm). (b) Corresponding EQE spectra of these devices. The extinction coefficients of SubPc and C_{70} in arbitrary unit are shown for comparison.

Table 1. Photovoltaic parameters of the OPV devices with various C_{70} thicknesses.

Device	V_{OC} (V)	J_{SC} (mA cm^{-2})	FF (%)	PCE (%)
10 nm	1.02	4.8	54	2.7
20 nm	1.03	6.1	57	3.6
30 nm	1.05	6.5	61	4.2
40 nm	1.04	5.4	59	3.3

To confirm our inference of the improved J_{SC} being attributed to the optical effect, we calculated the optical-field distribution for layer structures with different C_{70} thicknesses using the transfer matrix method.[73] For simplicity, the light is assumed to propagate normal to the device. The optical constants for each layer, as obtained from Fig. 1(b), are used for the calculation. Figs. 4(a) and 4(b) compare the optical-field profiles in terms of the normalized intensity $|E_0|^2$ inside the devices at wavelengths of 585 nm and 500 nm, respectively; these wavelengths chosen here correspond to the highest absorption for SubPc and C_{70}, respectively. The solid lines indicate the SubPc/C_{70} interface at which the excitons are efficiently dissociated into free carriers. In Fig. 4, the first optical interference maximum from the cathode occurs at a very different position in spite of a small change in C_{70} thickness for each incident wavelength and device structure, implying the importance of the thickness and optical optimization in bi-layer devices. For the wavelength of 585 nm, where the SubPc primarily absorbs, the maximum $|E_0|^2$ shifts from the ITO/MoO_3 interface to the C_{70}/BCP interface with increasing C_{70} thickness, indicating that the optimum optical-field distribution is achieved by the 30-nm C_{70}, as shown in Fig. 4(a). At the wavelength of 500 nm, which corresponds to the highest absorption of C_{70}, both the optical-field intensity and the position are quite different. The C_{70} with a thickness of 40 nm is found to provide the most desirable profile but the lowest $|E_0|^2$ at the SubPc/C_{70} interface, while the other devices exhibit comparable optical-field intensities at this interface. These results, however, are insufficient to explain the observed trend in J_{SC} because the difference in $|E_0|^2$ at the SubPc/C_{70} interface is insignificant for each data set. The energy or power dissipation in the active layers, which is highly dependent on the extinction coefficient of the absorbing layer, should be taken into account, in particular, the obvious differences in the absorption property between SubPc and C_{70}, as shown in Fig. 1(b).

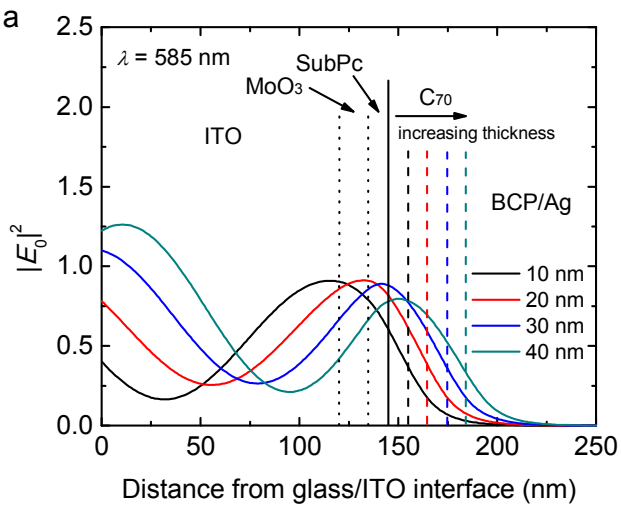

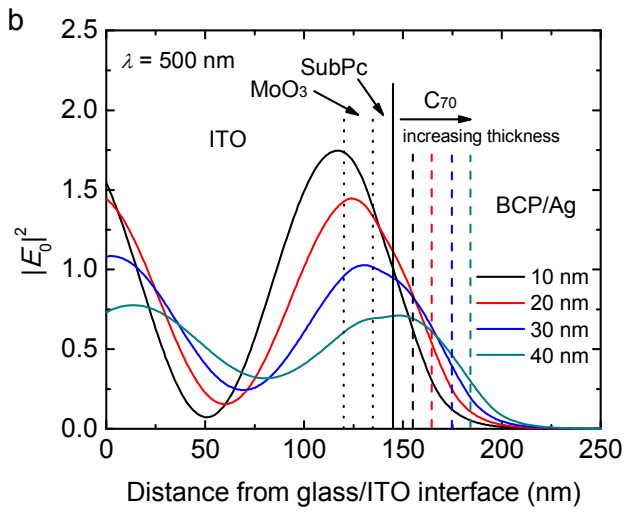

Fig. 4. Calculated optical-field distribution inside the OPV devices with different C_{70} thicknesses for the light wavelengths of (a) 585 nm and (b) 500 nm. $|E_0|^2$ denotes the optical-field intensity normalized by the incident light. The vertical solid lines indicate the interface between SubPc and C_{70}. The vertical dashed lines indicate the C_{70}/BCP interface. The vertical dotted lines differentiate the interfaces at ITO/MoO_3 and MoO_3/SubPc.

The power dissipation, $Q(z, \lambda)$, in the material at a distance z from the glass/ITO surface can be calculated by[45, 69, 73]

$$Q(z,\lambda) = \frac{1}{2} c\varepsilon_0 \alpha n |E_0|^2, \qquad (2)$$

where c is the speed of light, α is the absorption coefficient, and n is the refractive index; under AM 1.5G solar illumination with an intensity of 100 mW cm^{-2}, the power dissipation has a unit of W m^{-2} nm^{-1}.[69, 93] Fig. 5 shows the absorption profiles represented by $Q(z, \lambda)$ for layer structures with different C_{70} thicknesses at the wavelengths of 500 nm and 585 nm. Note that the abrupt changes in α and n between different materials cause the discontinuity at each interface. In contrast to the optical-field distribution, the power dissipation profile is considerably different, depending on both the wavelength and position. By incorporating the material absorption properties into the optical conditions inside the device, it becomes possible to obtain clear insight into the change in J_{SC} for different structures. In the SubPc and C_{70} layers, the power dissipation is mainly dominated by the wavelengths of 585 and 500 nm, respectively, corresponding to the peak absorption of each material. As the thickness of C_{70} increases, the shape of the power dissipation in SubPc varies greatly, revealing maximum shifts from the MoO_3/SubPc interface to the SubPc/C_{70} interface. To obtain a large number of free carriers that are dissociated from photo-induced excitons, the power dissipated at the donor/acceptor interface should be as high as possible, especially in a bi-layer having only a limited dissociation site.[94-96] Alternatively, the maximum power dissipation must be located very close to the donor/acceptor interface at which only excitons can separate into free carriers. From these aspects, the C_{70} thickness of 30 nm is expected to give the highest photocurrent generated from the SubPc layer at the wavelength of 585 nm. In contrast, the total power dissipated in C_{70} increases with its thickness at the wavelength of 500 nm. Because previous reports have shown that the exciton diffusion length is shorter in C_{70} than in C_{60} as reflected by a lower FF,[38, 42, 70] it is inferred that only the excitons generated close to the SubPc/C_{70} interface can contribute to the photocurrent. Therefore, the J_{SC} originates from C_{70} that are comparable except when the C_{70} thickness exceeds 40 nm, which exhibits a greatly reduced power dissipation.

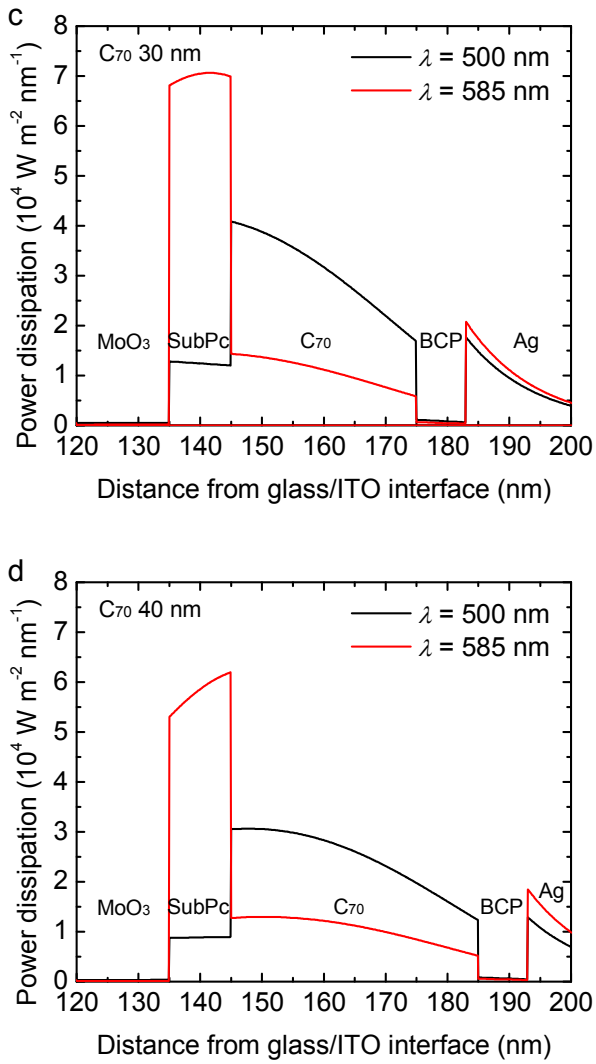

Fig. 5. Power dissipation as a function of layer thickness inside the devices with (a) 10-nm, (b) 20-nm, (c) 30-nm, and (d) 40-nm C_{70}. Black and red lines represent the distribution at the incident wavelengths of 500 nm and 585 nm, respectively.

Fig. 6(a) shows the relationship between the experimental J_{SC} and the optical-field intensity at the SubPc/C_{70} interface for the OPV devices with various C_{70} thicknesses. The additional devices with C_{70} layer thickness of 50 nm and 60 nm were also fabricated and compared. The J_{SC} becomes smaller when the C_{70} thickness increases as a result of the inferior optical-field distribution and the deteriorated electrical property. At the wavelength of 585 nm, corresponding to the absorption peak of SubPc, the predicted optical-field intensity is consistent with the experimental J_{SC}. For the absorption peak of C_{70}, at the wavelength of 500 nm, the prediction disagrees with the experimental result when the thickness of C_{70} is less than 30 nm. This result suggests that the theoretical J_{SC} may be overestimated if the absorption property of the material is not taken into account. To address this issue, the power dissipation at the SubPc/C_{70} interface is compared to the experimental J_{SC}

at various C_{70} thicknesses, as shown in Fig. 6(b). For the incident wavelength at 585 nm, the experimental data agree well with the calculation. When the incident wavelength is 500 nm, the power dissipation is reduced more than at the wavelength of 585 nm, implying the reduced contribution of C_{70} to the photocurrent compared with SubPc. As a result, the trend in J_{SC} is primarily dominated by the SubPc and has a minor relation to the C_{70}. Nevertheless, tuning the thickness of C_{70} favors the optical manipulation inside the OPV devices, providing a simple way to optimize the J_{SC} of bi-layer devices without losing the electrical property and hence the FF. In our case, we successfully improved the J_{SC} while maintaining a high V_{OC} and FF, leading to an enhanced PCE from 2.7 to 4.2%, with a V_{OC} of 1.05 V, J_{SC} of 6.5 mA cm^{-2}, and FF of 0.61. This result is highly efficient among the state-of-the-art bi-layer OPV devices based on small molecules without further treatments or structural designs.

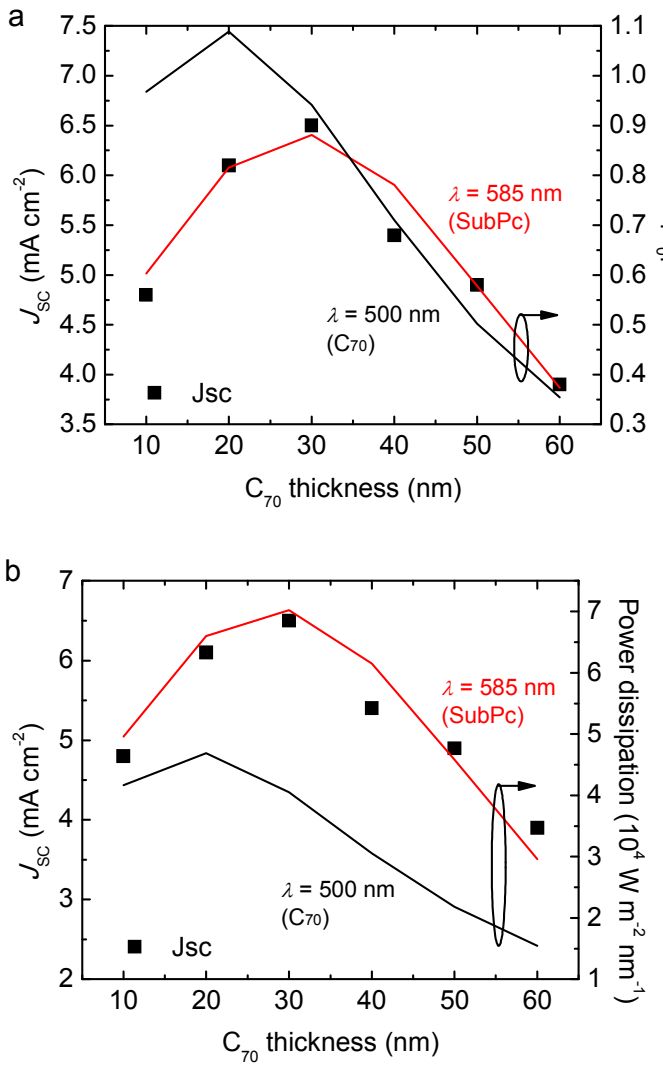

Fig. 6. Comparisons of the experimental J_{SC} with the calculated (a) optical-field intensity and (b) power dissipation at the SubPc/C_{70} interface as a function of C_{70} thickness. Black and red lines represent the calculated values at the wavelengths of 500 nm and 585 nm, respectively. The text in parentheses indicates the principally absorbing material at such wavelengths.

The above results indicated that the optical-field distribution of OPV devices was optimized by changing the thickness of C_{70} without the compensation of electrical properties. From Fig. 2(b), it is expected that the electrical properties could be further optimized by changing the SubPc thickness, as the carrier mobility of SubPc is significantly lower than C_{70}. Fig. 7(a) shows the *J-V* characteristics in the dark for the OPV devices with varied SubPc thicknesses: 5 nm, 10 nm, 15 nm, and 20 nm. The forward current is considerably decreased at a thicker SubPc, indicating the reduction in carrier transport and hence the reduction in electrical properties. The R_S was determined in the same manner as used to extract the diode behavior in Fig. 2(a), showing R_S of 2.6 Ω cm^2, 3.9 Ω cm^2, 5.4 Ω cm^2, and 11.4 Ω cm^2 for the devices with 5-nm, 10-nm, 15-nm, and 20-nm SubPc, respectively. This result highlights the dominance of a low-mobility material in the electrical properties of OPV devices. The corresponding photo *J-V* characteristics are shown in the inset in Fig. 7(a). Table 2 summarizes the photovoltaic parameters of these devices. Except for the 5-nm SubPc device, the J_{SC} and FF are decreased with the thickness of SubPc, as a result of the increased R_S caused by poor carrier transport. This opposite trend in J_{SC} observed for the device with the 5-nm SubPc is ascribed to the exciton quench in the case without using an anodic exciton blocking layer.[44, 97, 98] For the devices with SubPc thicknesses exceeding 15 nm, the diode behavior becomes deviated from the ideal case and an *s*-shape emerges, which is generally caused by the combination of an imbalance in the carrier mobility and an inappropriate active layer thickness.[75, 99] In addition, the thickness-dependent V_{OC} is also observed, which is attributed to the potential change inside the device as a result of the hole and electron accumulation at the anode and cathode interface, thus leading to the increased built-in potential (V_{bi}) and hence the V_{OC}.[49, 75, 99] To gain insight into this aspect, we measured the capacitance-voltage (*C-V*) characteristics of these devices with different SubPc thicknesses, as shown in Fig. 7(b). The *C-V* characteristic is generally described by the Mott-Schottky relation[100]

$$C^{-2} = \frac{2(V_{bi} - V)}{A^2 e \varepsilon \varepsilon_0 N_A}, \qquad (3)$$

where A is the device active area, e is the elementary charge, and N_A is the p-type doping concentration. The V_{bi} estimated from the low-voltage onset point is 0.79 V, 0.85 V, 0.91 V, and 0.97 V for the devices with 5-nm, 10-nm, 15-nm, and 20-nm SubPc, respectively. This result is consistent with the observed trend in the experimental V_{OC} but is not necessarily a reflection of the realistic value because the V_{OC} can depend on charge accumulation inside the device, which likely dominates the recombination losses in our case.[75] Therefore, the V_{OC} loss becomes increasingly serious the thicker the SubPc layer is, as observed from the experimental V_{OC}. The p-type doping concentration derived from Eq. (3) is 4.9 × 10^{16}, 3.6 × 10^{16}, 2.7 × 10^{16}, and 2.2 × 10^{16} cm^{-3} for the device with 5-nm, 10-nm, 15-nm, and 20-nm SubPc, respectively, by assuming that ε is 3.9 for SubPc.[101, 102] Although it is not well understood how the p-type doping concentration affects the device performance, several reports have indicated improved device performance as the p-type doping concentration decreased.[103, 104] Nevertheless, as inferred from the V_{bi} result, a serious carrier recombination originating from the charge accumulation is in turn detrimental to the device performance. As a result, the charge accumulation comes at the expense of the J_{SC} and FF, and therefore, an optimized SubPc thickness is found to be approximately 10 nm. Given the already optimized optical condition, the electrical property is further optimized by the donor thickness. Our result

represents a comprehensive and systematic study on the thickness optimization process in bi-layer OPV devices with the decoupling of the optical and electrical properties.

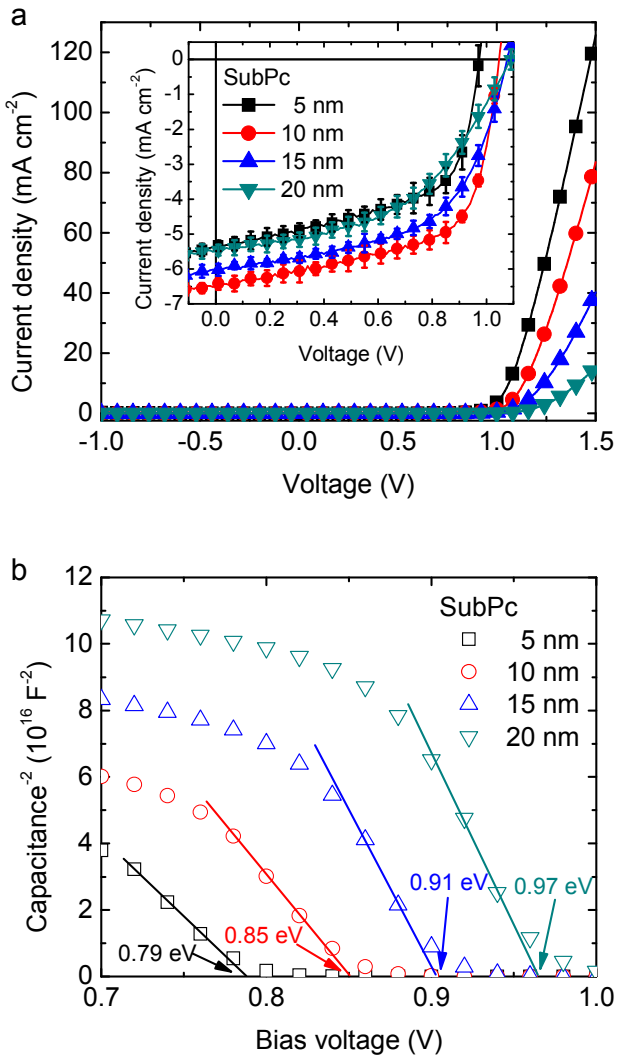

Fig. 7. (a) *J-V* characteristics in the dark for devices with varied SubPc thicknesses in the structure of ITO/MoO_3 (15 nm)/SubPc/C_{70} (30 nm)/BCP (8 nm)/Ag (100 nm). The inset is the corresponding photocurrent measured under AM 1.5G solar illumination. (b) *C-V* characteristics measured with 100 mV ac signal and 1 kHz frequency in the dark for the corresponding devices with various SubPc thicknesses. The solid lines indicate the region used to calculate the p-type doping concentration.

Table 2. Photovoltaic performances of the devices with various SubPc thicknesses.

Device	V_{OC} (V)	J_{SC} (mA cm^{-2})	FF (%)	PCE (%)	R_S (Ω cm^2)*
5 nm	0.97	5.3	58	3.0	2.6
10 nm	1.05	6.4	62	4.2	3.9
15 nm	1.08	6.0	56	3.6	5.4
20 nm	1.09	5.4	48	2.9	11.4

*R_S is determined by fitting the experimental dark current to the generalized diode equation; detailed information is described in the ESI ‡ (Section S1).

Experimental

Device fabrication

All materials, namely MoO_3, SubPc, C_{70}, and BCP, were purchased from Sigma-Aldrich. The organic materials SubPc and BCP were purified twice prior to use. The purification process was performed in a home-build thermal-gradient sublimation system, which consists of a heating zone with three regions at different temperatures in an outer quartz tube equipped with a vacuum system (pressure < 10^{-6} Torr) as provided in ESI‡ (Section S2). The material was placed in a quartz container and positioned in the first region at a temperature higher than the sublimation temperature of the material of interest. The second and third regions are at gradually decreased temperatures to allow vaporized material for deposition on the wall of the inner quartz tube. The heavy impurities and other substances remained in the quartz container, whereas the lighter impurities went far from the quartz container and deposited at the end of the inner quartz tube. The middle of the inner quartz tube containing the purified material is then cut away with a diamond tip tube cutter to avoid mixing materials from different regions during the removal of the purified material. A standard photolithography process was used to pattern the ITO slides as provided in ESI‡ (Section S3). Before the device fabrication, the ITO substrates were soaked in consecutive solutions, detergent, deionized water, acetone, and isopropanol, and under ultrasonic bath for 10 min in each step. The OPV devices were fabricated onto pre-patterned ITO glass substrates with a sheet resistance of approximately 10 Ω/sq. The pattern allowed us to produce five devices on one substrate. The ITO substrates were cleaned using solutions in an ultrasonic bath. After the cleaning process, the substrates were transferred into a high vacuum chamber (< 8 × 10^{-6} Torr) without further treatments. Before the deposition of the cathode, all the thin films were deposited layer-by-layer instead of mixing into a blend or mixture. A chamber with a home-made independently controlled shutter system to fabricate at most four cell parameters without breaking the vacuum, resulting in the minimization of the deviations due to device-to-device and run-to-run differences. The deposition of the Ag cathode through a shadow mask defines the active area of 0.04 cm^2. The thickness of each layer was calibrated with a series of thickness measurements using a surface profiler (Veeco Dektak 3) and an ellipsometry (Raditech SE-950). The deposition rates of all layers were monitored using a quartz crystal microbalance and were well-controlled to within 0.1-0.2 nm/s during the deposition process. After the device fabrication, an encapsulation process involving a UV-curable epoxy resin and a getter-attached cover glass was used to avoid degradation from exposure to the ambient environment. A total number of 10 devices on two different substrates for each cell parameter were produced. Detailed information on the device pattern and encapsulation is provided in the ESI‡ (Section S4).

Device characterization

All of the measurements were performed in air. The photo *J-V* characteristics were determined using a sourcemeter (Keithley 2400) to record the current under voltage bias and a solar simulator (Newport 91160A) for the AM 1.5G illumination at an intensity of 100 mW cm^{-2}, which was calibrated using a silicon reference cell (PV measurement area = 3.981 cm^2). The EQE spectra were determined using a lock-in amplifier (Stanford Research Systems SR830) chopped at 250 Hz to measure the photocurrent of devices under the monochromatic light illumination from a monochromator (Newport 74100). Note that the EQE spectra were verified by integrating the product of the EQE data and the AM 1.5G solar spectrum to extract the theoretical J_{SC}, which exhibits an error of less than 3% compared with the experimental J_{SC}. The HOMO levels and the work functions of the thin films were estimated using a photoelectron spectrometer (Riken Keiki AC-2). The energy gaps of the materials were evaluated from the high-energy onset point in the absorption spectra collected using a UV-visible spectrophotometer (Thermo Scientific Evolution 220). The optical constants for each layer were measured using an ellipsometry, as was used in determining the film thickness. *C-V* characteristics were determined using a Precision LCR Meter (Agilent E4980A) with a 100 mV ac signal and a frequency of 1 kHz.

Conclusions

In summary, we demonstrated that the considerable imbalance of carrier mobility between SubPc and C_{70} is not detrimental to the device performance, which enables one to manipulate and optimize the optical conditions by changing the C_{70} thickness without influencing the electrical properties. The simultaneously increased J_{SC}, V_{OC}, and FF improve the device efficiency from 2.7 to 4.2% at an optimal C_{70} thickness in small-molecule bi-layer OPV devices. The optical-tuning effects upon the change in C_{70} thickness are systematically studied by means of the optical-field intensity and power dissipation profiles inside the OPV device. It is found that the optical-field intensity at the dissociation interface is insufficient in predicting the trend in J_{SC}. The absorption properties of active layers should be involved in the calculation to take into account the power dissipation. As a result, the power dissipated at the SubPc/C_{70} interface is in good agreement with the experimental J_{SC}, proving the importance of optimization of the acceptor layer thickness. Upon the thickness change in a low-mobility donor, the electrical properties of OPV devices were significantly affected, either by the poor charge transport or the carrier recombination, as observed from the *C-V* characteristics. Our result provides a simple method of achieving high-performance bi-layer OPV devices and for predicting the correlation between the optical effects and the photocurrent.

Acknowledgements

The authors acknowledge the financial support from the National Science Council (Grant Nos. NSC 102-2221-E-131-026-MY2, 102-2221-E-131-030-MY2, 102-2221-E-011-142, 102-2511-S-131-002, 102-2622-E-011-018-CC3, 103-ET-E-011-004-ET, 103-2627-E-002-002, and 103-2622-E-131-007-CC3). In addition, one of the authors (S.-W. Liu) thanks Mr. H.-H. Wu, Syskey Technology Corporation (Taiwan), for the assistance in the fabrication of the designed system.

Notes and references

[a]Department of Electronic Engineering, National Taiwan University of Science and Technology, Taipei 10607, Taiwan, Republic of China. E-mail: cclee@mail.ntust.edu.tw

[b]Department of Electronic Engineering, Ming Chi University of Technology, New Taipei City 24301, Taiwan, Republic of China. E-mail: swliu@mai.mcut.edu.tw

†These two authors contributed equally to this work.

‡ Electronic Supplemental Information (ESI) available: Further information on the device pattern and encapsulation, as well as the diode properties for all studied OPV devices.

1 M. Kaltenbrunner, M. S. White, E. D. Głowacki, T. Sekitani, T. Someya, N. S. Sariciftci and S. Bauer, *Nat. Commun.*, 2012, **3**, 770.

2 M. J. Beliatis, K. K. Gandhi, L. J. Rozanski, R. Rhodes, L. McCafferty, M. R. Alenezi, A. S. Alshammari, C. A. Mills, K. D. G. I. Jayawardena, S. J. Henley and S. R. P. Silva, *Adv. Mater.*, 2014, **26**, 2078-2083.

3 N. Espinosa, M. Hosel, M. Jorgensen and F. C. Krebs, *Energy Environ. Sci.*, 2014, **7**, 855-866.

4 F. Machui, M. Hosel, N. Li, G. D. Spyropoulos, T. Ameri, R. R. Sondergaard, M. Jorgensen, A. Scheel, D. Gaiser, K. Kreul, D. Lenssen, M. Legros, N. Lemaitre, M. Vilkman, M. Valimaki, S. Nordman, C. J. Brabec and F. C. Krebs, *Energy Environ. Sci.*, 2014, **7**, 2792-2802.

5 L. Dou, J. You, J. Yang, C.-C. Chen, Y. He, S. Murase, T. Moriarty, K. Emery, G. Li and Y. Yang, *Nat. Photon.*, 2012, **6**, 180-185.

6 Z. He, C. Zhong, S. Su, M. Xu, H. Wu and Y. Cao, *Nat. Photon.*, 2012, **6**, 591-595.

7 C. E. Small, S. Chen, J. Subbiah, C. M. Amb, S.-W. Tsang, T.-H. Lai, J. R. Reynolds and F. So, *Nat. Photon.*, 2012, **6**, 115-120.

8 R. A. J. Janssen and J. Nelson, *Adv. Mater.*, 2013, **25**, 1847-1858.

9 N. Li, D. Baran, K. Forberich, F. Machui, T. Ameri, M. Turbiez, M. Carrasco-Orozco, M. Drees, A. Facchetti, F. C. Krebs and C. J. Brabec, *Energy Environ. Sci.*, 2013, **6**, 3407-3413.

10 T. R. Andersen, H. F. Dam, B. Andreasen, M. Hösel, M. V. Madsen, S. A. Gevorgyan, R. R. Søndergaard, M. Jørgensen and F. C. Krebs, *Sol. Energy Mater. Sol. Cells*, 2014, **120, Part B**, 735-743.

11 T. R. Andersen, H. F. Dam, M. Hösel, M. Helgesen, J. E. Carlé, T. T. Larsen-Olsen, S. A. Gevorgyan, J. W. Andreasen, J. Adams and N. Li, *Energy Environ. Sci.*, 2014, **7**, 2925-2933.

12 D. Angmo, P. M. Sommeling, R. Gupta, M. Hösel, S. A. Gevorgyan, J. M. Kroon, G. U. Kulkarni and F. C. Krebs, *Adv. Eng. Mater.*, 2014, **16**, 976-987.

13 J. E. Carle, M. Helgesen, M. V. Madsen, E. Bundgaard and F. C. Krebs, *J. Mater. Chem. C*, 2014, **2**, 1290-1297.

14 C. W. Schlenker and M. E. Thompson, *Chem. Commun.*, 2011, **47**, 3702-3716.

15 Y. Lin, Y. Li and X. Zhan, *Chem. Soc. Rev.*, 2012, **41**, 4245-4272.

16 C. W. Tang, *Appl. Phys. Lett.*, 1986, **48**, 183-185.

17 P. Peumans and S. Forrest, *Appl. Phys. Lett.*, 2001, **79**, 126-128.

18 T. Taima, M. Chikamatsu, Y. Yoshida, K. Saito and K. Yase, *Appl. Phys. Lett.*, 2004, **85**, 6412-6414.

19 C.-W. Chu, Y. Shao, V. Shrotriya and Y. Yang, *Appl. Phys. Lett.*, 2005, **86**, 243506.
20 A. K. K. Kyaw, D. H. Wang, V. Gupta, W. L. Leong, L. Ke, G. C. Bazan and A. J. Heeger, *ACS Nano*, 2013, **7**, 4569-4577.
21 Y. Liu, C.-C. Chen, Z. Hong, J. Gao, Y. M. Yang, H. Zhou, L. Dou, G. Li and Y. Yang, *Sci. Rep.*, 2013, **3**, 3356.
22 J. Zhou, Y. Zuo, X. Wan, G. Long, Q. Zhang, W. Ni, Y. Liu, Z. Li, G. He and C. Li, *J. Am. Chem. Soc.*, 2013, **135**, 8484-8487.
23 X. Che, X. Xiao, J. D. Zimmerman, D. Fan and S. R. Forrest, *Adv. Energy Mater.*, 2014, in press.
24 Y.-H. Chen, C.-W. Chen, Z.-Y. Huang, K.-T. Wong, L.-Y. Lin, F. Lin and H.-W. Lin, *Org. Electron.*, 2014, **15**, 1828-1835.
25 Y. Zou, J. Holst, Y. Zhang and R. J. Holmes, *J. Mater. Chem. A*, 2014, **2**, 12397-12402.
26 K. Cnops, B. P. Rand, D. Cheyns, B. Verreet, M. A. Empl and P. Heremans, *Nat. Commun.*, 2014, **5**, 3406.
27 W. J. Potscavage, A. Sharma and B. Kippelen, *Acc. Chem. Res.*, 2009, **42**, 1758-1767.
28 M. Zhang, H. Wang, H. Tian, Y. Geng and C. W. Tang, *Adv. Mater.*, 2011, **23**, 4960-4964.
29 G. Chen, H. Sasabe, Z. Wang, X.-F. Wang, Z. Hong, Y. Yang and J. Kido, *Adv. Mater.*, 2012, **24**, 2768-2773.
30 S.-W. Chiu, L.-Y. Lin, H.-W. Lin, Y.-H. Chen, Z.-Y. Huang, Y.-T. Lin, F. Lin, Y.-H. Liu and K.-T. Wong, *Chem. Commun.*, 2012, **48**, 1857-1859.
31 B. Walker, A. B. Tamayo, X. D. Dang, P. Zalar, J. H. Seo, A. Garcia, M. Tantiwiwat and T. Q. Nguyen, *Adv. Funct. Mater.*, 2009, **19**, 3063-3069.
32 S. Loser, C. J. Bruns, H. Miyauchi, R. P. Ortiz, A. Facchetti, S. I. Stupp and T. J. Marks, *J. Am. Chem. Soc.*, 2011, **133**, 8142-8145.
33 S. Loser, H. Miyauchi, J. W. Hennek, J. Smith, C. Huang, A. Facchetti and T. J. Marks, *Chem. Commun.*, 2012, **48**, 8511-8513.
34 A. Mishra and P. Bäuerle, *Angew. Chem. Int. Ed.*, 2012, **51**, 2020-2067.
35 S. B. Darling and F. You, *Rsc Advances*, 2013, **3**, 17633-17648.
36 H.-J. Song, J. Y. Kim, D. Lee, J. Song, Y. Ko, J. Kwak and C. Lee, *J. Nanosci. Nanotechnol.*, 2013, **13**, 7982-7987.
37 R. Pandey and R. J. Holmes, *Adv. Mater.*, 2010, **22**, 5301-5305.
38 R. Pandey, Y. Zou and R. J. Holmes, *Appl. Phys. Lett.*, 2012, **101**, 033308.
39 Z. Wang, D. Yokoyama, X.-F. Wang, Z. Hong, Y. Yang and J. Kido, *Energy Environ. Sci.*, 2013, **6**, 249-255.
40 D. Cheyns, B. P. Rand and P. Heremans, *Appl. Phys. Lett.*, 2010, **97**, 033301.
41 S. Sista, Z. Hong, L.-M. Chen and Y. Yang, *Energy Environ. Sci.*, 2011, **4**, 1606-1620.
42 B. E. Lassiter, J. D. Zimmerman, A. Panda, X. Xiao and S. R. Forrest, *Appl. Phys. Lett.*, 2012, **101**, 063303.
43 B. Verreet, P. E. Malinowski, B. Niesen, D. Cheyns, P. Heremans, A. Stesmans and B. P. Rand, *Appl. Phys. Lett.*, 2013, **102**, 043301.
44 S. Grob, M. Gruber, A. N. Bartynski, U. Hörmann, T. Linderl, M. E. Thompson and W. Brütting, *Appl. Phys. Lett.*, 2014, **104**, 213304.
45 N.-K. Persson, M. Schubert and O. Inganäs, *Sol. Energy Mater. Sol. Cells*, 2004, **83**, 169-186.
46 D. P. Gruber, G. Meinhardt and W. Papousek, *Sol. Energy Mater. Sol. Cells*, 2005, **87**, 215-223.
47 M. Lenes, L. J. A. Koster, V. D. Mihailetchi and P. W. M. Blom, *Appl. Phys. Lett.*, 2006, **88**, 243502.
48 D. W. Sievers, V. Shrotriya and Y. Yang, *J. Appl. Phys.*, 2006, **100**, 114509.
49 P. Kumar, H. Kumar, S. Jain, P. Venkatesu, S. Chand and V. Kumar, *Jpn. J. Appl. Phys.*, 2009, **48**, 121501.
50 T. Kirchartz, T. Agostinelli, M. Campoy-Quiles, W. Gong and J. Nelson, *J. Phys. Chem. Lett.*, 2012, **3**, 3470-3475.
51 M. Y. Chan, S. L. Lai, K. M. Lau, C. S. Lee and S. T. Lee, *Appl. Phys. Lett.*, 2006, **89**, 163515.
52 J. Y. Kim, S. H. Kim, H. H. Lee, K. Lee, W. Ma, X. Gong and A. J. Heeger, *Adv. Mater.*, 2006, **18**, 572-576.
53 J. Gilot, I. Barbu, M. M. Wienk and R. A. Janssen, *Appl. Phys. Lett.*, 2007, **91**, 113520.
54 K. H. An, B. O'Connor, K. P. Pipe and M. Shtein, *Org. Electron.*, 2009, **10**, 1152-1157.
55 R. Schueppel, R. Timmreck, N. Allinger, T. Mueller, M. Furno, C. Uhrich, K. Leo and M. Riede, *J. Appl. Phys.*, 2010, **107**, 044503.
56 B. V. Andersson, D. M. Huang, A. J. Moule and O. Inganäs, *Appl. Phys. Lett.*, 2009, **94**, 043302.
57 D. J. Pinner, R. H. Friend and N. Tessler, *J. Appl. Phys.*, 1999, **86**, 5116-5130.
58 K. L. Mutolo, E. I. Mayo, B. P. Rand, S. R. Forrest and M. E. Thompson, *J. Am. Chem. Soc.*, 2006, **128**, 8108-8109.
59 V. Shrotriya, G. Li, Y. Yao, C.-W. Chu and Y. Yang, *Appl. Phys. Lett.*, 2006, **88**, 073508.
60 J. Sakai, T. Taima, T. Yamanari and K. Saito, *Sol. Energy Mater. Sol. Cells*, 2009, **93**, 1149-1153.
61 K. Kawano and C. Adachi, *Appl. Phys. Lett.*, 2010, **96**, 053307.
62 A. P. Yuen, N. M. Bamsey, A.-M. Hor, J. S. Preston, R. A. Klenkler, S. M. Jovanovic and R. O. Loutfy, *Sol. Energy Mater. Sol. Cells*, 2011, **95**, 3137-3141.
63 I. Hancox, P. Sullivan, K. V. Chauhan, N. Beaumont, L. A. Rochford, R. A. Hatton and T. S. Jones, *Org. Electron.*, 2010, **11**, 2019-2025.
64 M. D. Perez, C. Borek, S. R. Forrest and M. E. Thompson, *J. Am. Chem. Soc.*, 2009, **131**, 9281-9286.
65 X. Tong, B. E. Lassiter and S. R. Forrest, *Org. Electron.*, 2010, **11**, 705-709.
66 X. Xi, W. Li, J. Wu, J. Ji, Z. Shi and G. Li, *Sol. Energy Mater. Sol. Cells*, 2010, **94**, 2435-2441.
67 M. Vogel, S. Doka, C. Breyer, M. C. Lux-Steiner and K. Fostiropoulos, *Appl. Phys. Lett.*, 2006, **89**, 163501.
68 H. Gommans, B. Verreet, B. P. Rand, R. Muller, J. Poortmans, P. Heremans and J. Genoe, *Adv. Funct. Mater.*, 2008, **18**, 3686-3691.
69 F. Monestier, J.-J. Simon, P. Torchio, L. Escoubas, F. Flory, S. Bailly, R. de Bettignies, S. Guillerez and C. Defranoux, *Sol. Energy Mater. Sol. Cells*, 2007, **91**, 405-410.
70 F. Monestier, J.-J. Simon, P. Torchio, L. Escoubas, B. Ratier, W. Hojeij, B. Lucas, A. Moliton, M. Cathelinaud, C. Defranoux and F. Flory, *Appl. Opt.*, 2008, **47**, C251-C256.
71 A. Hadipour, B. de Boer and P. W. M. Blom, *J. Appl. Phys.*, 2007, **102**, 074506.
72 A. Roy, S. Heum Park, S. Cowan, M. H. Tong, S. Cho, K. Lee and A. J. Heeger, *Appl. Phys. Lett.*, 2009, **95**, 013302.

73 L. A. A. Pettersson, L. S. Roman and O. Inganas, *J. Appl. Phys.*, 1999, **86**, 487-496.
74 B. O'Connor, K. H. An, K. P. Pipe, Y. Zhao and M. Shtein, *Appl. Phys. Lett.*, 2006, **89**, 233502.
75 C.-C. Lee, W.-C. Su, S.-W. Liu and C.-H. Yuan, *Jpn. J. Appl. Phys.*, 2012, **51**, 09MA04.
76 T.-Y. Chu and O.-K. Song, *Appl. Phys. Lett.*, 2007, **90**, 203512.
77 M. A. Khan, W. Xu, H. Khizar ul, Y. Bai, X. Y. Jiang, Z. L. Zhang, W. Q. Zhu, Z. L. Zhang and W. Q. Zhu, *J. Appl. Phys.*, 2008, **103**, 014509.
78 R. Pandey, A. A. Gunawan, K. A. Mkhoyan and R. J. Holmes, *Adv. Funct. Mater.*, 2012, **22**, 617-624.
79 R. F. Salzman, J. Xue, B. P. Rand, A. Alexander, M. E. Thompson and S. R. Forrest, *Org. Electron.*, 2005, **6**, 242-246.
80 C.-F. Lin, S.-W. Liu, C.-C. Lee, J.-C. Hunag, W.-C. Su, T.-L. Chiu, C.-T. Chen and J.-H. Lee, *Sol. Energy Mater. Sol. Cells*, 2012, **103**, 69-75.
81 S.-W. Liu, W.-C. Su, C.-C. Lee, C.-C. Chou and C.-W. Cheng, *ECS Solid State Lett.*, 2012, **1**, P70-P72.
82 S.-W. Liu, W.-C. Su, C.-C. Lee, C.-W. Cheng, C.-C. Chou and C.-F. Lin, *J. Electrochem. Soc.*, 2013, **160**, G14-G18.
83 S.-W. Liu, W.-C. Su, C.-C. Lee, C.-W. Cheng, C.-C. Chou and C.-F. Lin, *Jpn. J. Appl. Phys.*, 2013, **52**, 041602.
84 S. Pfuetzner, J. Meiss, A. Petrich, M. Riede and K. Leo, *Appl. Phys. Lett.*, 2009, **94**, 223307.
85 M. Zhang, H. Wang and C. W. Tang, *Appl. Phys. Lett.*, 2010, **97**, 143503.
86 A. Wilke, J. Endres, U. Hörmann, J. Niederhausen, R. Schlesinger, J. Frisch, P. Amsalem, J. Wagner, M. Gruber, A. Opitz, A. Vollmer, W. Brütting, A. Kahn and N. Koch, *Appl. Phys. Lett.*, 2012, **101**, 233301.
87 D. Cheyns, J. Poortmans, P. Heremans, C. Deibel, S. Verlaak, B. P. Rand and J. Genoe, *Phys. Rev. B*, 2008, **77**, 165332.
88 A. Maurano, R. Hamilton, C. G. Shuttle, A. M. Ballantyne, J. Nelson, B. O'Regan, W. Zhang, I. McCulloch, H. Azimi, M. Morana, C. J. Brabec and J. R. Durrant, *Adv. Mater.*, 2010, **22**, 4987-4992.
89 K. Vandewal, K. Tvingstedt, A. Gadisa, O. Inganäs and J. V. Manca, *Phys. Rev. B*, 2010, **81**, 125204.
90 S. Ko, E. T. Hoke, L. Pandey, S. Hong, R. Mondal, C. Risko, Y. Yi, R. Noriega, M. D. McGehee, J.-L. Brédas, A. Salleo and Z. Bao, *J. Am. Chem. Soc.*, 2012, **134**, 5222-5232.
91 Y. Zhao, Z. Xie, C. Qin, Y. Qu, Y. Geng and L. Wang, *Sol. Energy Mater. Sol. Cells*, 2009, **93**, 604-608.
92 R. Pandey and R. J. Holmes, *Appl. Phys. Lett.*, 2012, **100**, 083303.
93 N.-K. Persson, H. Arwin and O. Inganas, *J. Appl. Phys.*, 2005, **97**, 034503.
94 B. A. Gregg and M. C. Hanna, *J. Appl. Phys.*, 2003, **93**, 3605-3614.
95 B. Kippelen and J.-L. Bredas, *Energy Environ. Sci.*, 2009, **2**, 251-261.
96 Y. Zheng and J. Xue, *Polym. Rev.*, 2010, **50**, 420-453.
97 M. Hirade and C. Adachi, *Appl. Phys. Lett.*, 2011, **99**, 153302.
98 J. D. Zimmerman, B. Song, O. Griffith and S. R. Forrest, *Appl. Phys. Lett.*, 2013, **103**, 243905.
99 W. Tress, A. Petrich, M. Hummert, M. Hein, K. Leo and M. Riede, *Appl. Phys. Lett.*, 2011, **98**, 063301.
100 G. Garcia-Belmonte, A. Munar, E. M. Barea, J. Bisquert, I. Ugarte and R. Pacios, *Org. Electron.*, 2008, **9**, 847-851.
101 H. Gommans, D. Cheyns, T. Aernouts, C. Girotto, J. Poortmans and P. Heremans, *Adv. Funct. Mater.*, 2007, **17**, 2653-2658.
102 H. Gommans, S. Schols, A. Kadashchuk, P. Heremans and S. Meskers, *J. Phys. Chem. C*, 2009, **113**, 2974-2979.
103 E. Meijer, A. Mangnus, B.-H. Huisman, G. t Hooft, D. De Leeuw and T. Klapwijk, *Synth. Met.*, 2004, **142**, 53-56.
104 M. Glatthaar, M. Riede, N. Keegan, K. Sylvester-Hvid, B. Zimmermann, M. Niggemann, A. Hinsch and A. Gombert, *Sol. Energy Mater. Sol. Cells*, 2007, **91**, 390-393.

